

Disorder-Driven Collapse of Topological Phases in Photonic Topological Insulator

Hongfang Zhang,* Wenjie Sui, Yu Zhang, Gangcheng Liu, Qiang Shi, Zengtao Lv, Dong Zhang, Chucai Rong, and Bing Yang*

By embedding the position disorder of rods in 2D gyromagnetic photonic crystal, the influences of increasing random disorder on the photonic topological phases (PTPs) in a photonic topological insulator are numerically investigated. When the disorder is small, the PTPs almost have no change. With the increase in disorder, the PTPs at the edge of the original topological bandgap are first affected, and those at center of the bandgap have the best robustness. As disorder increases to a critical value, the PTPs collapse ultimately. During the collapse of the PTPs, disorders can induce the Anderson localization of electromagnetic (EM) wave, and produce localized hot spots in the system. When the disorder is not too large, the hot spots are excited at the edge area near the excitation source, and have little influence on the one-way propagation of the topological edge state (TES). As disorder increases continuously, the hot spots would penetrate the system deeply and affect the propagation of EM waves significantly, which leads to the collapse of the PTPs and destruction of one-way propagation of TES. Even so, there are still remaining long-range and short-range orders in the system. This research provides a theoretical model and an experiment platform for further studying the relationship between topological phases and disorders.

physical applications.^[7–14] Till now, many kinds of topological phases have been proposed and designed theoretically and experimentally in different physical systems.^[15–30]

Although there have been lots of studies on topological phases in physics, most of them were implemented in periodic structures, which have translational symmetry with both long-range and short-range positional orders.^[31–41] The topological phases in periodic structures can be studied by calculating the topological index (such as Chern number, Z_2 index) of the band structures in reciprocal space.^[42–45] However, disorders are ubiquitous in nature, and various kinds of disorders, such as position disorder, structure disorder, and composition disorder, will inevitably be introduced in device productions. The existence of disorders will affect or even change the properties of topological phases in periodic structures.^[46–49] Moreover, in the aspect of the theory, the relationship between topological

phases and disorders is also a fundamental problem in physics, which is of great significance for a deep understanding of the formation, evolution, and modulation of topological phases.^[50–52]

So far, researchers have theoretically studied some topological phases in electronic systems containing disorders.^[53,54] Moreover, it was reported that disorders could even induce topological Anderson insulators in trivial systems.^[55–57] However, due to the limitation of electronic systems themselves, it is impossible to accurately modulate disorders in electronic structures in reality. Therefore, the researches about electronic topological phases containing disorders are hard to be verified in experiment. Compared with the electronic system, the photonic system has good controllability. We can accurately control the kind and strength of disorders needed in the system in reality. To date, the influence of disorders on the PTPs has been studied in some photonic systems theoretically and experimentally,^[58–61] and even the topological Anderson insulators of EM wave have been designed and observed by analogy with the tight-binding approximation model of the electronic system.^[62] Nonetheless, the influence of increasing disorder on the PTPs in photonic micro-nano structures containing multiple scattering of EM waves is not very clear up to now.^[63–66]


In this article, by embedding the position disorder of rod elements in 2D gyromagnetic photonic crystal (GPhC), we

1. Introduction

Topological phases in physics were first observed in 2D electron gas in the 1980s.^[1,2] In 2008, Haldane et al. extended the concept of topological phases to the field of optics, and initiated the field of topological photonics.^[3] Due to their fascinating properties, such as supporting topological edge state (TES) with one-way propagation and robustness against impurities or defects at the edge area,^[4–6] the topological phases in physics have important applications in electronics, photonics, and other

H. Zhang, W. Sui, Y. Zhang, G. Liu, Q. Shi, Z. Lv, D. Zhang, B. Yang
Shandong Provincial Key Laboratory of Optical Communication Science and Technology
School of Physical Science and Information Engineering
Liaocheng University
Liaocheng 252059, China
E-mail: zhanghongfang1@lcu.edu.cn; yangbing@lcu.edu.cn

C. Rong
School of Physics and Electronic Information
Gannan Normal University
Ganzhou 341000, China

 The ORCID identification number(s) for the author(s) of this article can be found under <https://doi.org/10.1002/pssb.202200214>.

DOI: 10.1002/pssb.202200214

numerically investigate the influence of increasing random disorder on the PTPs in photonic topological insulators containing multiple scattering of EM waves. Our results show that disorder will collapse the PTPs gradually as disorder strength increases continuously. When disorder strength is small, the PTPs are robust. With the increase in disorder, the competition between Anderson localization and PTPs forms a kind of hybrid state. The hybrid state can form localized hot spots of EM waves at the edge area of the system near the excitation source, and these hot spots have little influence on the one-way propagation of TES at first. As disorder strength continues to increase, the hybrid state will extend into the system, and the hot spots will also penetrate deeply into the system. At this time, the one-way propagation of TES will be degraded significantly. Finally, when the disorder reaches a critical value, the PTPs will be completely collapsed, and the one-way propagation of TES will become indistinguishable. Even so, there are still recognizable long-range and short-range orders in the system. Our study is different from previous works concerning the topological phase transition in photonic crystals.^[21,52,59] In Refs.[21] and [52], the authors studied the topological edge transport in amorphous magnetic photonic crystals. In an amorphous system, there is no long-range order while the short-range order still exists. In Ref. [59], the authors investigated the disorder-induced topological state transition in photonic chiral hyperbolic metamaterial which is not easy to implement in the experiment. Our study is helpful for understanding the relationship between topological phase and disorder, and our design can also be easily realized and verified in experiment.

2. Theoretical Model and Disorder Design

In our studies, the theoretical model of the photonic topological insulator without disorder is a 2D square lattice GPhC composed of gyromagnetic rods immersed in the air with an external DC magnetic field along rod axes (z -direction). The lattice constant of the photonic crystal is a and the rod radius is R , as shown in **Figure 1e**. The relative permeability tensor of the gyromagnetic rod takes the form of

$$\vec{\mu}_r = \begin{bmatrix} \mu_r & i\kappa_r & 0 \\ -i\kappa_r & \mu_r & 0 \\ 0 & 0 & 1 \end{bmatrix} \quad (1)$$

with i the imaginary unit. The μ_r and κ_r are determined by rod components, mode frequency, and external DC magnetic field.^[15] For simplicity, we neglect the effects of material dispersion and loss, assuming a constant permeability tensor with real-valued μ_r and κ_r for a particular external magnetic field. The relative permittivity of the rod is ϵ_r , and permeability and permittivity of the air background take the values of μ_0 and ϵ_0 , respectively, as in a vacuum. Here, we set $\mu_r = 1$, $\kappa_r = 0.4$, $\epsilon_r = 13$, and $R = 0.13a$,^[21,42] and only mode with an electric field parallel to the rod axes is considered.

When there is no disorder, the topological phases can be investigated by calculating the Chern numbers of the band structure in reciprocal space, and the Chern number of bandgap can be obtained by summing the Chern numbers of all bands below

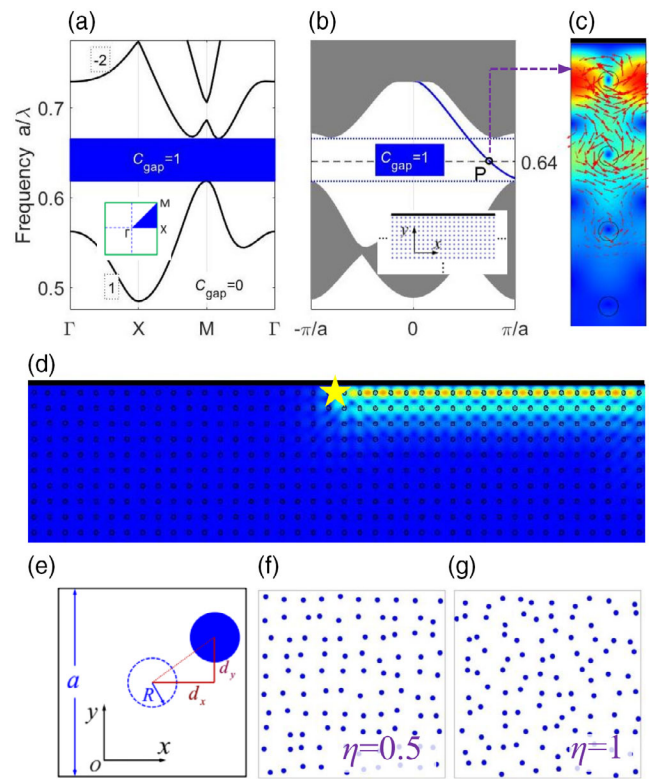


Figure 1. a) Band structure of the gyromagnetic photonic crystal (GPhC). Chern numbers of bands and bandgaps are marked. Insert is the first Brillouin zone. b) Projected band diagram when the GPhC is terminated on the upper side by a metallic boundary. The topological edge state (TES) is denoted with a blue solid curve. Insert is the calculation model. c) Eigenmode field of the TES of point P. Red arrows denote the Poynting vector. d) One-way propagation of the TES stimulated by point source denoted with a yellow star. e) Position disorder of rod in each primitive cell. A dashed (solid) circle denotes rod position without (with) disorder. f, g) Sketch maps of disordered GPhC within a region of $10a \times 10a$ as η takes 0.5 and 1, respectively. Blue dots are rod elements.

the bandgap.^[44] Figure 1a shows the band structure of the model within the frequency range from $a/\lambda = 0.475$ to 0.775 , together with the Chern numbers of the bands and bandgaps marked in the figure. Here λ is the wavelength in the air background. Clearly, there exists a complete topological bandgap (blue region) with Chern number $C_{\text{gap}} = 1$ within the frequency range from $a/\lambda = 0.618$ to 0.666 . According to the bulk-boundary correspondence theorem,^[42–45] there will be a TES at the edge area if the GPhC is terminated with boundaries.

In Figure 1b, we show the projected band diagram when the GPhC is terminated on the upper side by a metallic boundary along the x -direction,^[42] which constructs a semi-infinite structure of the GPhC in the y -direction (still periodic in the x -direction, see the inset in Figure 1b). Clearly, corresponding to the topological bandgap $C_{\text{gap}} = 1$ in Figure 1a, there exists a single-mode gapless TES (blue solid curve) only with negative group velocity denoting its one-way propagation in Figure 1b. The two dotted blue lines denote the top and bottom of the complete topological bandgap and the dashed black line marks

the center of the bandgap with a frequency of $a/\lambda = 0.64$. Figure 1c shows the eigenmode field of the TES at the frequency of $a/\lambda = 0.64$ marked by point P in Figure 1b, with the red arrows denoting the flow of EM energy (Poynting vector). Obviously, the TES is mainly confined at the edge area within a distance of about $2a$ from the metallic boundary and only moves to the right. Figure 1d shows the propagation of the TES at point P in Figure 1b stimulated by a point excitation source in this semi-infinite structure. The point source is denoted by the yellow star and the black line on the upper side of the system is the metallic boundary. Clearly, the EM radiation is confined at the edge area and only propagates to the right.

To embed disorder, we introduce random displacements to the rod positions in GPhC, defined as

$$d_{x(y)}^i = \eta \xi_{x(y)}^i (a - 2R) \quad (2)$$

for the i th rod along x (y) direction as shown in Figure 1e, where the dashed (solid) circle denotes the rod position without (with) disorder in a primitive cell. Here, η is a parameter quantitatively describing the disorder strength from 0 to 1, and $\xi_{x(y)}^i$ is a random number with a uniform distribution between -0.5 and 0.5 .^[58] A set of $\xi_{x(y)}^i$ of all the rods in the model determines

a single disorder configuration (SDC) $\{\xi_{x(y)}^i\}$ of the system. In our studies, the SDC is randomly generated at each disorder strength η as it increases from $\eta = 0$ to 1 continuously. Figure 1f,g show the sketch maps of the GPhC at $\eta = 0.5$ and 1 with different SDC, respectively, within a region of $10a \times 10a$. Obviously, the embedded disorder breaks down the translation symmetry of the system.

3. Numerical Results and Discussions

3.1. Influence of Disorder on the Topological Bandgap

With the increase in disorder strength η , the translation symmetry is destroyed, and both the long-range and short-range orders of the system are changed. The reciprocal space cannot be defined and the frequency band structure cannot be calculated. Therefore, we first calculate the localization length L_{loc} (with COMSOL Multiphysics) in real space to examine the influence of disorder on the change of the topological bandgap. The calculation model without disorder is shown in Figure 2a, which contains a rectangular region in GPhC, as shown as the area in the violet box R_b , including $N_x \times N_y = 40 \times 17 = 680$ rods with

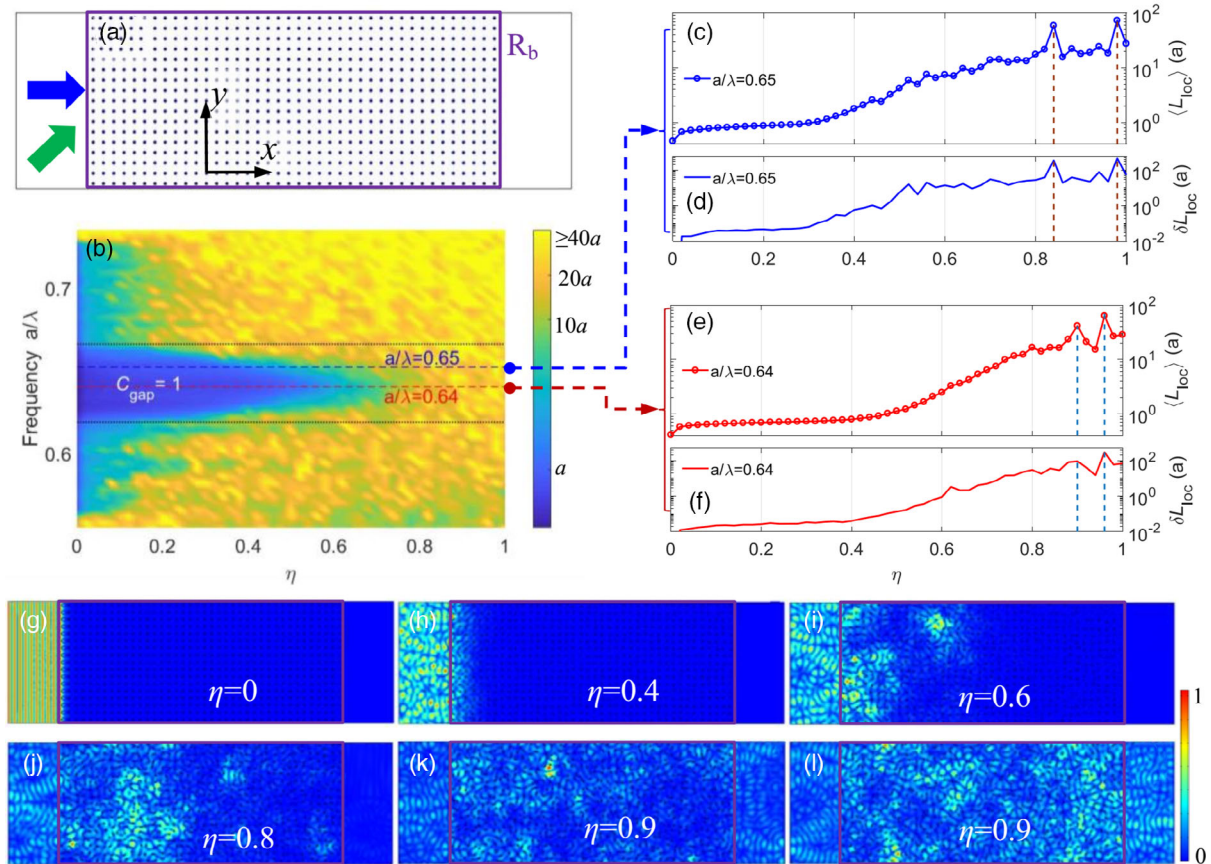


Figure 2. a) Calculation model for localization length L_{loc} without the disorder. Blue dots are rods. b) Results of $\log(\langle L_{loc} \rangle/a)$ with increases of η . Two black dotted lines denote the topological bandgap of Figure 1a. c–f) Statistic average of localization length $\langle L_{loc} \rangle$ and standard deviation δL_{loc} at frequencies of $a/\lambda = 0.65$ and 0.64 , respectively. g–l) Simulations of propagation of electromagnetic (EM) wave ($|E_z|$) at a frequency of $a/\lambda = 0.64$ when $\eta = 0, 0.4, 0.6, 0.8$, and 0.9 (with different single disorder configurations (SDCs)), respectively.

N_x (N_y) the number of rods in x (y) direction. Without loss of generality, here we calculate the localization length L_{loc} when the incident wave travels in the x -direction, denoted by the blue arrow in the figure, corresponding to the ΓX direction in reciprocal space when there is no disorder. By setting the left and right boundaries (in the x -direction) of the rectangular region R_b as the input and output ports respectively, and the upper and lower boundaries (in the y -direction) periodic, the localization length L_{loc} can be obtained by

$$L_{loc} = -\frac{N_x \times a}{\ln T} \quad (3)$$

with T the transmittance of the system in the x -direction.^[65]

The statistic average of localization length $\langle L_{loc} \rangle$ is shown in Figure 2b with $\langle \cdot \cdot \cdot \rangle$ representing the average of 100 random SDCs at each disorder strength η . For a clear comparison, we take the logarithmic results of $\langle L_{loc} \rangle$ in the figure, and mark the $\langle L_{loc} \rangle$ greater than $40a$ with the same color as that of the $\langle L_{loc} \rangle$ equal to $40a$. The two black dotted lines denote the top and bottom of the complete bandgap in Figure 1a, denoting the topological bandgap within the frequency range from $a/\lambda = 0.618$ to 0.666 without the disorder, and the blue and red dashed lines denote the frequencies at $a/\lambda = 0.65$ and 0.64 , respectively.

As can be seen from Figure 2b, when there is no disorder, the $\langle L_{loc} \rangle$ is very small ($\approx a$) within the frequency range from about $a/\lambda = 0.56$ to 0.73 , which corresponds to the bandgap along the ΓX direction of the band structure in Figure 1a. Within this frequency range, the EM wave cannot propagate from left to right (in the x -direction) in the system. With the embedding of disorder and increase of disorder strength η , the $\langle L_{loc} \rangle$ increases rapidly at frequencies outside the complete bandgap and possesses robustness within the frequency range inside the complete bandgap. As η increases further, $\langle L_{loc} \rangle$ in the complete bandgap also changes significantly. The $\langle L_{loc} \rangle$ at the edge of the bandgap gets a rapid increase first, and then $\langle L_{loc} \rangle$ at center of the bandgap has the best robustness to disorder, which indicates that the PTPs at the edge of the topological bandgap are more susceptible to the disorder than those at the center. When the disorder strength η is large enough, the $\langle L_{loc} \rangle$ in the entire complete bandgap can reach about $20a$. At this time, the EM wave can pass partly through the system from left to right, thus the topological bandgap is collapsed. To see this more clearly, in Figure 2c,e, we show the $\langle L_{loc} \rangle$ at frequencies of $a/\lambda = 0.65$ and 0.64 , respectively, with an increase of η . Figure 2d,f is their corresponding standard deviations δL_{loc} . In Figure 2g–l, we show the simulation examples of the wave propagation in the system with different disorder strength η at a frequency of $a/\lambda = 0.64$.

From Figure 2c (Figure 2e), the results of $\langle L_{loc} \rangle$ at frequency of $a/\lambda = 0.65$ ($a/\lambda = 0.64$), we can see that when the η increases to about $\eta = 0.3$ ($\eta = 0.5$), the $\langle L_{loc} \rangle$ begins to increase rapidly, and when the η increases to about $\eta = 0.6$ and 0.7 ($\eta = 0.7$ and 0.8), the $\langle L_{loc} \rangle$ reaches about $10a$ and $20a$, respectively. So, it is clear that the $\langle L_{loc} \rangle$ at the center of the topological bandgap ($a/\lambda = 0.64$) is more robust to disorder. From the results of standard deviations δL_{loc} in Figure 2d,f, it can be seen that the δL_{loc} gradually increases with an increase of η , and after η is greater than a critical value (about $\eta = 0.5$ at $a/\lambda = 0.65$ and $\eta = 0.65$ at $a/\lambda = 0.64$, respectively), the δL_{loc} is close to and then greater than the

corresponding $\langle L_{loc} \rangle$. This indicates that as the η increases continuously, the localizations of EM waves caused by a disorder in different SDCs with the same η are becoming more and more different. In addition, the $\langle L_{loc} \rangle$ can obtain very large values at some disorder strengths. For example, the $\langle L_{loc} \rangle$ can reach about $59a$ and $73a$ at $\eta = 0.84$ and 0.98 when $a/\lambda = 0.65$, and $41a$ and $63a$ at $\eta = 0.9$ and 0.96 when $a/\lambda = 0.64$, respectively, as shown as the locations of η at dashed lines in Figure 2c,e. The reason is that, for a certain SDC with disorder strength η , the incident EM wave can stimulate local hot spots near the out port of the simulation model (see an example of Figure 2l), which results in a much larger transmittance T , and hence a much larger L_{loc} of this particular SDC than those of other SDCs with the same η . As a result, the $\langle L_{loc} \rangle$ will get a large value, and correspondingly, the δL_{loc} at this η also get a large value, as shown in Figure 2c–f.

Figure 2g–l shows the simulation examples of propagation of EM wave ($|E_z|$) in the system at a frequency of $a/\lambda = 0.64$ when $\eta = 0$, $\eta = 0.4$, $\eta = 0.6$, $\eta = 0.8$, and $\eta = 0.9$ (with different SDCs), respectively. When $\eta = 0$, i.e., there is no disorder, the incident wave is completely reflected at the input port, indicating that the system is a good insulator now. When $\eta = 0.4$ and $\eta = 0.6$, part of the incident wave enters the system and forms some localized hot spots near the input port. These hot spots gradually penetrate the system with an increase of η . When $\eta = 0.8$, the hot spot region is significantly deeper into the system than when $\eta = 0.4$ and 0.6 . Figure 2k,l is the results of two different SDCs with $\eta = 0.9$. It can be seen that in both cases the EM wave is diffused throughout the system. So the topological bandgap in Figure 1a vanishes now. In addition, the local hot spot in Figure 2l is located near the out port, which results in a very large T , and hence a very large L_{loc} ($1587a$). This is what causes the sudden increase of $\langle L_{loc} \rangle$ and δL_{loc} at $\eta = 0.9$ in Figure 2e,f.

Therefore, with an increase of η , the disorder-induced localization will form some hot spots close to the excitation source in the system first, and then, with a further increase of η , these hot spots will gradually extend deeply into the system, thus changing the propagation of EM wave. When the η is large enough, the propagation of the EM wave will eventually collapse the topological bandgap, and also the PTSs of the system.

We also calculate the L_{loc} of the system when the incident wave goes along the direction of the green arrow shown in Figure 2a, corresponding to the ΓM direction in reciprocal space when there is no disorder. The same conclusions can be obtained from the aforementioned studies. As η increases continuously in the system, the ΓX and ΓM directions in the reciprocal space become indistinguishable gradually, and the transmissions of EM waves along different directions become the same little by little. The details are shown in Supporting Information.^[67]

3.2. Influence of Disorder on the TES

According to the characteristics of TES, i.e., edge confinement and one-way propagation of the EM wave, we define two parameters, named edge confinement parameter C_e and one-way propagation parameter P_r , to study the influence of disorder on the TES.^[52,59] The C_e is used to determine the quality of the localization of the EM wave at the edge area of the system, and the P_r is used to determine the quality of the

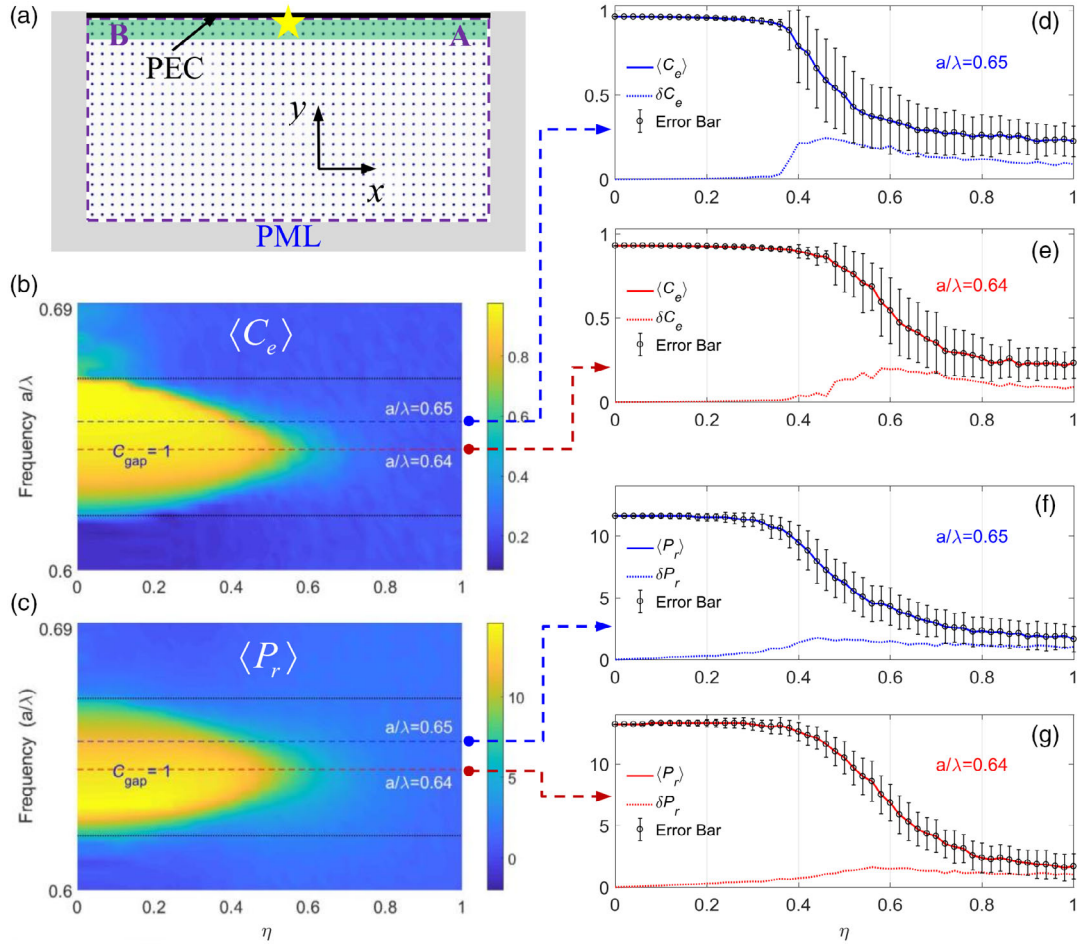


Figure 3. a) Calculation model for edge confinement parameter C_e and one-way propagation parameter P_r . Black solid line is a metallic boundary (perfect electrical conductivity (PEC)). Perfect matched layer (PML) is shown as a gray area. Point source is denoted with the yellow star. Π_e (green area) and Π (region in violet dashed box) represent the edge area and the whole area of the GPhC, respectively. Points A and B are the locations of energy density measurements. b,c) Statistic averages $\langle C_e \rangle$ and $\langle P_r \rangle$ with increases of η . Two black dotted lines denote the topological bandgap of Figure 1a. d–g) $\langle C_e \rangle$ and $\langle P_r \rangle$, and their standard deviations δC_e and δP_r at frequencies of $a/\lambda = 0.65$ and 0.64 , respectively.

one-way propagation of the EM wave. **Figure 3a** shows the calculation model, a finite GPhC structure containing $N_x \times N_y = 40 \times 20 = 800$ rods with N_x (N_y) the number of rods in the x (y) direction. The upper side of the structure is covered with a metallic boundary that acts as a perfect electrical conductivity (PEC) to prevent the scattering of EM waves into the air area outside the system. The left, right, and lower regions of the structure are perfect matched layer (PML), used to absorb the EM wave incident on them and eliminate the interference caused by reflection. The point excitation source is placed between the PEC and the GPhC, as shown by the yellow star in the figure.

The edge confinement parameter C_e is defined as

$$C_e = \frac{\int_{\Pi_e} \Omega(x, y) dx dy}{\int_{\Pi} \Omega(x, y) dx dy} \quad (4)$$

with $\Omega(x, y)$ the EM energy density at point (x, y) in the model.^[59] Π in the integral sign represents the whole area of the GPhC, surrounded by the violet dashed box in Figure 3a. Π_e is the edge

area denoted by the green region within a distance of $2a$ away from the PEC. $C_e \approx 1$ denotes the well-confined edge state, and the deviation of C_e from one implies the degradation of the edge confinement of EM radiation. According to the geometry of the model, if the EM radiation propagates freely in the system, C_e is approximately equal to 0.1.

The one-way propagation parameter P_r is defined as

$$P_r = \log \frac{\Omega_A}{\Omega_B} \quad (5)$$

with Ω_A (Ω_B) the EM energy density measured at point A (B),^[52] which is located at $17a$ to the right (left) of the point source and $a/2$ away from the PEC, as marked in Figure 3a. The larger the modulus of P_r is, the better the one-way propagation of the EM wave is. The positive or negative value of P_r represents the propagation of EM wave to A or B at the edge area, and $P_r = 0$ denotes the equal propagation of EM wave to A and B. The combination of C_e and P_r provides a detailed description of the influence of increasing random disorder on the TES in our photonic system.

The statistical averages of C_e and P_r , denoted with $\langle C_e \rangle$ and $\langle P_r \rangle$, are shown in Figure 3b,c, respectively. These results are obtained by averaging 100 different SDCs at each η . The two black dotted lines in the figure denote the top and bottom of the topological bandgap in Figure 1a,b, and the blue and red dashed lines denote the frequencies at $a/\lambda = 0.65$ and 0.64 , respectively. From the results of $\langle C_e \rangle$ and $\langle P_r \rangle$, it can be seen that in the case of weak disorder, $\langle C_e \rangle$ and $\langle P_r \rangle$ almost have no change with an increase of η at frequencies within the complete bandgap. As η increases continuously, the $\langle C_e \rangle$ and $\langle P_r \rangle$ at the edge of the complete bandgap get rapid decreases first, and then as η further increases, the $\langle C_e \rangle$ and $\langle P_r \rangle$ at the center of the bandgap get their rapid decreases too. The decreases of $\langle C_e \rangle$ and $\langle P_r \rangle$ indicate degradation of the edge confinement and one-way propagation of TES. When η is large enough, $\langle C_e \rangle$ can decrease to about 0.2 and $\langle P_r \rangle$ can decrease to about 2 at frequencies within the whole bandgap. At this time, the TES is collapsed, and the edge confinement and one-way propagation of EM waves cannot be distinguished any longer. Thus, the destruction of TES by increasing random disorder undergoes a gradual process, and the TES at the edge of the topological bandgap is more susceptible than those at entry of the bandgap.

To illustrate this more clearly, in Figure 3d–g, we show the $\langle C_e \rangle$ and $\langle P_r \rangle$ at frequencies of $a/\lambda = 0.65$ and 0.64 , respectively, together with their standard deviations denoted by error bars. At the same time, the values of standard deviations, denoted by δC_e and δP_r , are also plotted with dotted lines in each panel. In Figure 4, we show the simulation examples of the propagation of EM wave ($|E_z|$) in the system at the frequency of $a/\lambda = 0.64$ when $\eta = 0.2, 0.4, 0.5, 0.6, 0.7$, and 0.9 (with different SDC), respectively. From Figure 3d,f (Figure 3e,g) at a frequency of $a/\lambda = 0.65$ ($a/\lambda = 0.64$), it can be seen that $\langle C_e \rangle$ and $\langle P_r \rangle$ begin to decrease rapidly at about $\eta = 0.36$ ($\eta = 0.46$), and reach

their respective stable values of 0.2 and 2 at about $\eta = 0.7$ ($\eta = 0.8$). Clearly, the TES undergoes a gradual collapse, and the TES at the center of the bandgap is more robust to disorder.

From the results of standard deviations δC_e and δP_r in Figure 3d–g, it can also be seen that δC_e and δP_r in general experience a similar change with an increase of η . When the η is small, δC_e and δP_r are very small. With the continuous increase of η , δC_e and δP_r increase first, and then decrease gradually, and slowly approach their respective non-zero values at last. Taking the results of δC_e in Figure 3e at a frequency of $a/\lambda = 0.64$ as an example, we can see that δC_e is very small (≈ 0) before $\eta = 0.46$, and increases gradually from $\eta = 0.46$ to 0.6 , then slowly decreases from $\eta = 0.6$ to 0.8 , and ultimately tends to a nonzero value (≈ 0.1) after $\eta = 0.8$. The larger the standard deviation is, the greater the difference of EM wave propagation among different SDCs is. When $\eta < 0.46$, the TES confines most of the EM radiation at the edge area (see Figure 4a,b), and the C_e of different SDCs with the same η has little difference. When η increases from $\eta = 0.46$ to 0.6 , the hot spots caused by the disorder gradually enter the inner of the system near the edge area Π_e (such as H_1 in Figure 4c). In this way, different SDCs with the same η will generate localized hot spots at different localizations at the edge area Π_e or in the inner of the system near Π_e , leading to the increasing difference of C_e among different SDCs.^[68–70] When η increases from $\eta = 0.6$ to 0.8 , the hot spots gradually penetrate deeply into the inner of the system beyond Π_e (such as H_2 in Figure 4d and H_3 in Figure 4e), making the difference of C_e among different SDCs decreases according to the definition of C_e in Equation (4). After η is greater than 0.8 , the EM wave is diffused throughout the system and the hot spots are also randomly distributed in the whole structure Π (see Figure 4f), which leads to the stable value of δC_e about 0.2.

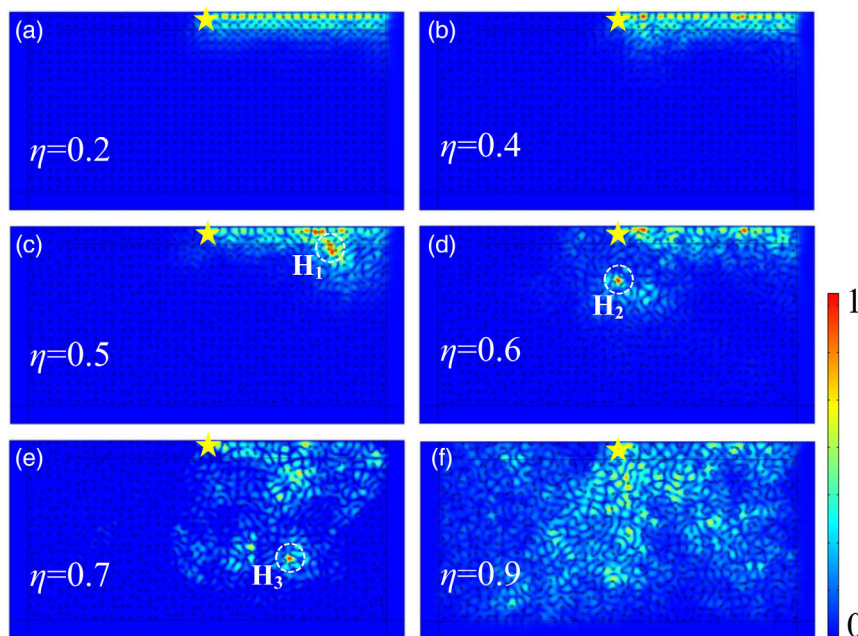


Figure 4. Simulations of propagation of EM wave ($|E_z|$) at a frequency of $a/\lambda = 0.64$ when $\eta = 0.2, 0.4, 0.5, 0.6, 0.7$, and 0.9 (with different SDC), respectively. Point source is denoted with a yellow star in each panel.

It should be noted that due to the EM wave localization caused by the disorder and the gyromagnetic effect of the rod itself, together with the statistical effects of the results, we think that when the $\langle C_e \rangle$ and $\langle P_r \rangle$ in Figure 3b,c reach about 0.2 and 2, respectively, the TES of the system has been collapsed already. This assertion can also be confirmed by comparing the values of $\langle C_e \rangle$ and $\langle P_r \rangle$ at frequencies inside and outside the complete bandgap in Figure 3b,c, respectively. In addition, in Supplemental Material, we give out a qualitative explanation to show these localized hot spots come from the Anderson localization of EM waves caused by the disorder.^[67] The aforementioned model is large enough to ensure the credibility of our research. To confirm this, as an example, we give out a scaling analysis of the results of $\langle C_e \rangle$ and $\langle P_r \rangle$ at the frequency of $a/\lambda = 0.64$ in Supporting Information.^[67] To show the influence of disorder on the TES along a bended edge, we also investigate the case of a U-shape edge and get the same conclusions as those obtained here. The detailed results are in Supporting Information.^[67]

3.3. Long-Range and Short-Range Orders During Collapse of the PTPs

For the periodic photonic topological insulators, there are both long-range and short-range positional orders in the system. Long-range order is connected to the lattice periodicity, and short-range order is related to the regular connectivity of

neighboring elements throughout the system. When the position disorders of rod elements are introduced, the translation periodicity of the system is broken and the neighboring connectivity in the underlying lattice is also changed.^[21,66] To investigate the change of long-range and short-range orders of the system during the collapse of the PTPs, we calculate the radial distribution function (RDF) of the system.^[66,71] For 2D systems, the RDF(r) can be obtained by

$$\text{RDF}(r)dr = \frac{1}{2\pi r N \rho} \sum_{i=1}^N \sum_{j=1}^N \langle \delta(r - r_{ij}) \rangle \quad (6)$$

where N is the number of the rod elements and ρ is the global rod density of the system. δ is the delta function and r_{ij} is the distance between two rod elements, $\langle \dots \rangle$ means the ensemble average. Randomly taking a rod as the origin, $\text{RDF}(r)dr$ gives the probability of finding a neighboring rod at a distance between r and $r+dr$. For a periodic structure with translation symmetry, long-range and short-range positional orders can be recognized by the presence of sharp peaks at large and small distances of r in the $\text{RDF}(r)$.

The RDF results of our model are shown in Figure 5 for disorder strength from $\eta = 0$ to 1 with an interval of $\eta = 0.2$, with the red curve denoting the statistic average $\langle \text{RDF} \rangle$ obtained by averaging 100 SDCs and the blue curve denoting the RDF of randomly selected an SDC at each η . From the results of $\langle \text{RDF} \rangle$,

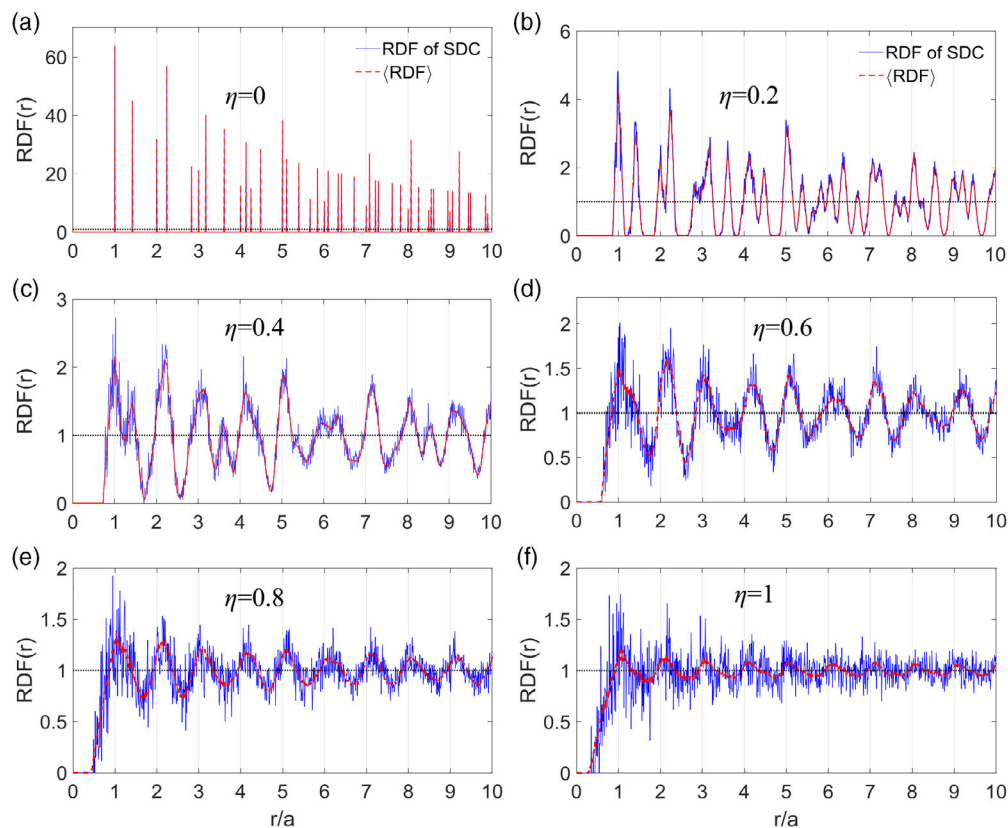


Figure 5. Radial distribution function (RDF) of the system for disorder strength from $\eta = 0$ to 1 with an interval of $\eta = 0.2$. Red curve denotes the statistic average $\langle \text{RDF} \rangle$ by averaging 100 SDCs and the blue curve denotes the RDF of a randomly selected SDC at each η in each panel.

it can be seen that as η increases continuously, both the short-range orders and long-range orders gradually merge into their adjacent orders at about integer multiples of lattice constant a , and the merged orders become weaker and weaker with an increase of η . However, even as η reaches its maximum value $\eta = 1$ when the PTPs have collapsed already, there are still recognizable short-range and long-range orders in the system. This kind of gradual change of short-range and long-range orders in the system is also consistent with the results obtained in Sections 3.1 and 3.2, where the PTPs are also gradually driven to collapse by increasing disorder.

It can also be seen from Figure 5 that when the η is small ($\eta = 0, 0.2$, and 0.4), the RDF (blue curve) of a randomly selected SDC is in good agreement with the statistic average $\langle \text{RDF} \rangle$ (red curve), denoting the little influence of small disorder on the orders of the system. With the increase of η , although the RDF of a randomly selected SDC is still consistent with the statistic average $\langle \text{RDF} \rangle$, on the whole, the fluctuations of RDF around $\langle \text{RDF} \rangle$ become more and more serious, which indicates the randomness of the orders of different SDCs at the same η . This kind of randomness is also reflected in the calculations and simulations of localization length and TES in Sections 3.1 and 3.2 as η increases to large values. However, the occurrence of Anderson localization of EM wave (hot spots) cannot be deduced from the results of RDF of a particular SDC. This may be due to the fact that the RDF is also a statistical average over all the lattices in a certain SDC, while the occurrence of Anderson localization of EM wave is an individual feature of details of rod positions in the system.

4. Conclusion

In this article, by calculating the localization length, edge confinement parameter, and one-way propagation parameter of 2D-disordered GPhC, we investigate the influence of increasing random disorder on the PTPs in a photonic topological insulator. The results show that the topological bandgap of the system, the edge confinement, and one-way propagation of the TES will be collapsed gradually as the disorder increases continuously. During the collapse of the PTPs, there exists a competition between Anderson localization and one-way propagation of TES in the system,^[68–70] leading to a hybrid state which has potential applications in topological resonators and topological random lasers.^[72–76] Although the PTPs are collapsed by the increasing disorder of rod positions, there are still remaining weak long-range and short-range orders in the system. Our numerical calculation provides a new path for the study of PTPs and our simulation model provides a theoretical example and an experiment platform for studying the PTPs containing disorders.

Supporting Information

Supporting Information is available from the Wiley Online Library or from the author.

Acknowledgements

H.Z. and W.S. contributed equally to this work. B.Y. thanks X.D.Z. for the helpful discussion. This work is supported by the Natural Science Foundations of Shandong Province of China (Grant No. ZR2021MA091) and Liaocheng University (Grant No. 318051705), the Research Fund from the MOE of China (Grant No. JZW17SL01). H.Z. thanks the Introduction and Cultivation Plan of Youth Innovation Talents for Universities of Shandong Province of China.

Conflict of Interest

The authors declare no conflict of interest.

Data Availability Statement

The data that support the findings of this study are available from the corresponding author upon reasonable request.

Keywords

disorder, photonic crystals, photonic topological insulator, topological edge state, topological phases

Received: May 13, 2022

Published online:

- [1] K. V. Klitzing, G. Dorda, M. Pepper, *Phys. Rev. Lett.* **1980**, *45*, 494.
- [2] D. C. Tsui, H. L. Stormer, A. C. Gossard, *Phys. Rev. Lett.* **1982**, *48*, 1559.
- [3] F. D. M. Haldane, S. Raghu, *Phys. Rev. Lett.* **2008**, *100*, 013904.
- [4] Z. Wang, Y. Chong, J. D. Joannopoulos, M. Soljačić, *Nature (London)* **2009**, *461*, 772.
- [5] A. B. Khanikaev, S. H. Mousavi, W. K. Tse, M. Kargarian, A. H. MacDonald, G. Shvets, *Nat. Mater.* **2013**, *12*, 233.
- [6] M. C. Rechtsman, J. M. Zeuner, Y. Plotnik, Y. Lumer, D. Podolsky, F. Dreisow, S. Nolte, M. Segev, A. Szameit, *Nature* **2013**, *496*, 196.
- [7] M. Z. Hasan, C. L. Kane, *Rev. Mod. Phys.* **2010**, *82*, 3045.
- [8] X.-L. Qi, S.-C. Zhang, *Rev. Mod. Phys.* **2011**, *83*, 1057.
- [9] A. Bansil, H. Lin, T. Das, *Rev. Mod. Phys.* **2016**, *88*, 021004.
- [10] C.-K. Chiu, J. C. Y. Teo, A. P. Schnyder, S. Ryu, *Rev. Mod. Phys.* **2016**, *88*, 035005.
- [11] Y. Wu, C. Li, X. Hu, Y. Ao, Y. Zhao, Q. Gong, *Adv. Opt. Mater.* **2017**, *5*, 1700357.
- [12] T. Ozawa, H. M. Price, A. Amo, N. Goldman, M. Hafezi, L. Lu, M. C. Rechtsman, D. Schuster, J. Simon, O. Zilberberg, I. Carusotto, *Rev. Mod. Phys.* **2019**, *91*, 015006.
- [13] Y. Chen, F. Meng, B. Jia, G. Li, X. Huang, *Phys. Status Solidi RRL* **2019**, *13*, 1900175.
- [14] H. Niu, S. Li, J. Zang, *Phys. Status Solidi RRL* **2020**, *14*, 2000338.
- [15] Z. Wang, Y. D. Chong, J. D. Joannopoulos, M. Soljačić, *Phys. Rev. Lett.* **2008**, *100*, 013905.
- [16] K. Fang, Z. Yu, S. Fan, *Nat. Photonics* **2012**, *6*, 782.
- [17] M. Hafezi, S. Mittal, J. Fan, A. Migdall, J. M. Taylor, *Nat. Photonics* **2013**, *7*, 1001.
- [18] L. Lu, C. Fang, L. Fu, S. G. Johnson, J. D. Joannopoulos, M. Soljačić, *Nat. Phys.* **2016**, *12*, 337.
- [19] J. Noh, S. Huang, D. Leykam, Y. D. Chong, K. P. Chen, M. C. Rechtsman, *Nat. Phys.* **2017**, *13*, 611.

- [20] B. Yang, Q. Guo, B. Tremain, R. Liu, L. E. Barr, Q. Yan, W. Gao, H. Liu, Y. Xiang, J. Chen, C. Fang, A. Hibbins, L. Lu, S. Zhang, *Science* **2018**, 359, 1013.
- [21] B. Yang, H. Zhang, T. Wu, R. Dong, X. Yan, X. Zhang, *Phys. Rev. B* **2019**, 99, 045307.
- [22] T. Zhang, Y. Jiang, Z. Song, H. Huang, Y. He, Z. Fang, H. Weng, C. Fang, *Nature (London)* **2019**, 566, 475.
- [23] M. G. Vergniory, L. Elcoro, C. Felser, N. Regnault, B. A. Bernevig, Z. Wang, *Nature* **2019**, 566, 480.
- [24] F. Tang, H. C. Po, A. Vishwanath, X. Wan, *Nature (London)* **2019**, 566, 486.
- [25] Y. Huang, S.-K. Jian, *Phys. Rev. B* **2021**, 103, L161113.
- [26] Y. Peng, B. Yan, J. Xie, E. Liu, H. Li, R. G. F. Gao, J. Liu, *Phys. Status Solidi RRL* **2020**, 14, 200202.
- [27] Y.-B. Yang, K. Li, L.-M. Duan, Y. Xu, *Phys. Rev. B* **2021**, 103, 085408.
- [28] J. Luo, Z. Du, Y. Guo, C. Liu, W. Zhang, X. Guo, *Nanophotonics* **2021**, 10, 4523.
- [29] K.-K. Om, K.-H. Kim, *Phys. Status Solidi RRL* **2022**, 16, 2100427.
- [30] Y. Yang, J. Lu, M. Yan, X. Huang, W. Deng, Z. Liu, *Phys. Rev. Lett.* **2021**, 126, 156801.
- [31] W.-J. Chen, S.-J. Jiang, X.-D. Chen, B. Zhu, L. Zhou, J.-W. Dong, C. T. Chan, *Nat. Commun.* **2014**, 5, 5782.
- [32] L.-H. Wu, X. Hu, *Phys. Rev. Lett.* **2015**, 114, 223901.
- [33] Z.-G. Chen, Y. Wu, *Phys. Rev. Appl.* **2016**, 5, 054021.
- [34] M. Yan, X. Huang, L. Luo, J. Lu, W. Deng, Z. Liu, *Phys. Rev. B* **2020**, 102, 180102.
- [35] J. Li, L. Wang, J. Liu, R. Li, Z. Zhang, X.-Q. Chen, *Phys. Rev. B* **2020**, 101, 081403.
- [36] C. Fu, Y. Sun, C. Felser, *APL Mater.* **2020**, 8, 040913.
- [37] W. Zhang, D. Zou, Q. Pei, W. He, J. Bao, H. Sun, X. Zhang, *Phys. Rev. Lett.* **2021**, 126, 146802.
- [38] M. S. Kirsch, Y. Zhang, M. Kremer, L. J. Maczewsky, S. K. Ivanow, Y. V. Kartashov, L. Torner, D. Bauer, A. Szameit, M. Heinrich, *Nat. Phys.* **2021**, 17, 995.
- [39] H. Liu, J.-K. Zhou, B.-L. Wu, Z.-Q. Zhang, H. Jiang, *Phys. Rev. B* **2021**, 103, 224203.
- [40] X. S. Wang, X. R. Wang, *J. Appl. Phys.* **2021**, 129, 151101.
- [41] M. J. Gilbert, *Commun. Phys.* **2021**, 4, 70.
- [42] S. A. Skirlo, L. Lu, M. Soljačić, *Phys. Rev. Lett.* **2014**, 113, 113904.
- [43] M. Hafezi, E. A. Demler, M. D. Lukin, J. M. Taylor, *Nat. Phys.* **2011**, 7, 907.
- [44] L. Lu, J. D. Joannopoulos, M. Soljačić, *Nat. Photonics* **2014**, 8, 821.
- [45] A. B. Khanikaev, G. Shvets, *Nat. Photonics* **2017**, 11, 763.
- [46] J. H. Bardarson, P. W. Brouwer, J. E. Moore, *Phys. Rev. Lett.* **2010**, 105, 156803.
- [47] E. Prodan, T. L. Hughes, B. A. Bernevig, *Phys. Rev. Lett.* **2010**, 105, 115501.
- [48] K. Kobayashi, T. Ohtsuki, K.-I. Imura, *Phys. Rev. Lett.* **2013**, 110, 236803.
- [49] J. H. García, L. Covaci, T. G. Rappoport, *Phys. Rev. Lett.* **2015**, 114, 116602.
- [50] P. Titum, N. H. Lindner, M. C. Rechtsman, G. Refael, *Phys. Rev. Lett.* **2015**, 114, 056801.
- [51] N. P. Mitchell, L. M. Nash, D. Hexner, A. M. Turner, W. T. M. Irvine, *Nat. Phys.* **2018**, 14, 380.
- [52] S. Mansha, Y. D. Chong, *Phys. Rev. B* **2017**, 96, 121405.
- [53] H. Huang, Y.-S. Wu, F. Liu, *Phys. Rev. B* **2021**, 101, 041103.
- [54] H.-B. Wu, J.-J. Liu, *Phys. Rev. B* **2021**, 103, 115430.
- [55] J. Li, R.-L. Chu, J. K. Jain, S.-Q. Shen, *Phys. Rev. Lett.* **2009**, 102, 136806.
- [56] C. W. Groth, M. Wimmer, A. R. Akhmerov, J. Tworzydło, C. W. J. Beenakker, *Phys. Rev. Lett.* **2009**, 103, 196805.
- [57] E. J. Meier, F. A. An, A. Dauphin, M. Maffei, P. Massignán, T. L. Hughes, B. Gadway, *Science* **2018**, 362, 929.
- [58] J. Lian, J.-X. Fu, L. Gan, Z.-Y. Li, *Phys. Rev. B* **2012**, 85, 125108.
- [59] C. Liu, W. Gao, B. Yang, S. Zhang, *Phys. Rev. Lett.* **2017**, 119, 183901.
- [60] B. Yang, H. Zhang, Q. Shi, T. Wu, Y. Ma, Z. Lv, X. Xiao, R. Dong, X. Yan, X. Zhang, *Opt. Express* **2020**, 28, 31487.
- [61] Y. Wang, Y.-H. Lu, J. Gao, Y.-J. Chang, H. Tang, X.-M. Jin, *Phys. Rev. B* **2021**, 103, 014110.
- [62] S. Stützer, Y. Plotnik, Y. Lumer, P. Titum, N. H. Lindner, M. Segev, M. C. Rechtsman, A. Szameit, *Nature* **2018**, 560, 461.
- [63] D. S. Wiersma, *Nat. Photonics* **2013**, 7, 188.
- [64] E. Maguid, M. Yannai, A. Faerman, I. Yulevich, V. Kleiner, E. Hasman, *Science* **2017**, 358, 1411.
- [65] G.-G. Liu, Y. Yang, X. Ren, H. Xue, X. Lin, Y.-H. Hu, H.-X. Sun, B. Peng, P. Zhou, Y. Chong, B. Zhang, *Phys. Rev. Lett.* **2020**, 125, 133603.
- [66] P. Zhou, G.-G. Liu, X. Ren, Y. Yang, H. Xue, L. Bi, L. Deng, Y. Chong, B. Zhang, *Light: Sci. Appl.* **2020**, 9, 133.
- [67] See Supporting Information for the results of L_{loc} along ΓM direction in reciprocal space, qualitative explanation of the Anderson localization of EM wave caused by disorder and scaling analysis of the results of $\langle C_e \rangle$ and $\langle P_r \rangle$ at the frequency of $a/\lambda = 0.64$.
- [68] M. Segev, Y. Silberberg, D. N. Christodoulides, *Nat. Photonics* **2013**, 7, 197.
- [69] H. H. Sheinfux, Y. Lumer, G. Ankonina, A. Z. Genack, G. Bartal, M. Segev, *Science* **2017**, 356, 953.
- [70] W. Schirmacher, B. Abaie, A. Mafi, G. Ruocco, M. Leonetti, *Phys. Rev. Lett.* **2018**, 120, 067401.
- [71] C. Jin, X. Meng, B. Cheng, Z. Li, D. Zhang, *Phys. Rev. B* **2001**, 63, 195107.
- [72] S. Schönhuber, M. Brandstetter, T. Hirsch, C. Deutsch, M. Krall, H. Detz, A. M. Andrews, G. Strasser, S. Rotter, K. Unterrainer, *Optica* **2016**, 3, 1035.
- [73] B. Abaie, E. Mobini, S. Karbasi, T. Hawkins, J. Ballato, A. Mafi, *Light: Sci. Appl.* **2017**, 6, e17041.
- [74] B. Babak, N. Abdoulaye, V. Felipe, E. A. Abdelkrim, F. Yeshaiah, K. Boubacar, *Science* **2017**, 358, 636.
- [75] G. Harari, M. A. Bandres, Y. Lumer, M. C. Rechtsman, Y. D. Chong, M. Khajavikhan, D. N. Christodoulides, M. Segev, *Science* **2018**, 359, eaar4003.
- [76] M. A. Bandres, S. Wittek, G. Harari, M. Parto, J. Ren, M. Segev, D. N. Christodoulides, M. Khajavikhan, *Science* **2018**, 359, eaar4005.